machines

Article

Model-Based Field Winding Interturn Fault Detection Method for Brushless Synchronous Machines

Kumar Mahtani [1], José M. Guerrero [2], Luis F. Beites [1] and Carlos A. Platero [1,*]

[1] Electrical Engineering Department, E.T.S. Ingenieros Industriales, Universidad Politécnica de Madrid, 28006 Madrid, Spain
[2] Energy and Fuels Department, E.T.S. Minas y Energía, Universidad Politécnica de Madrid, 28003 Madrid, Spain
* Correspondence: carlosantonio.platero@upm.es

Abstract: The lack of available measurements makes the detection of electrical faults in the rotating elements of brushless synchronous machines particularly challenging. This paper presents a novel and fast detection method regarding interturn faults at the field winding of the main machine, which is characterized because it is non-intrusive and because its industrial application is straightforward as it does not require any additional equipment. The method is built upon the comparison between the theoretical and the measured exciter field currents. The theoretical exciter field current is computed from the main machine output voltage and current magnitudes for any monitored operating point by means of a theoretical healthy brushless machine model that links the main machine with the exciter. The applicability of the method has been verified for interturn faults at different fault severity levels, both through computer simulations and experimental tests, delivering promising results.

Keywords: alternator; brushless excitation; brushless machine; condition monitoring; fault detection; power generation; power generator protection; protection system; synchronous machine

check for updates

Citation: Mahtani, K.; Guerrero, J.M.; Beites, L.F.; Platero, C.A. Model-Based Field Winding Interturn Fault Detection Method for Brushless Synchronous Machines. *Machines* **2022**, *10*, 1227. https://doi.org/10.3390/machines10121227

Academic Editor: Ahmed Abu-Siada

Received: 29 October 2022
Accepted: 13 December 2022
Published: 15 December 2022

1. Introduction

Wound field brushless synchronous machines (BSM) are largely used in power generation, besides many other applications, such as in aeronautical and marine fields [1–3]. They are gaining some ground as an alternative to permanent magnet synchronous machines, which have been largely studied [4], especially in small- and medium-sized motor and generator applications, and more concretely in electromobility and wind power generation, respectively.

The main advantage of BSM is the absence of brushes and slip rings in the excitation system [5]. As a result, maintenance requirements are reduced and safer operation is attained as spark production is avoided. In practice, common standards for AC power generators require that the protection systems of these machines shall guarantee power supply in a reliable way, but at the same time they shall trip the machine in case of an internal fault. In this regard, there are minimum requirements for fault protection [6].

There exist many BSM systems topologies for various applications [7–9]. These systems, as shown in Figure 1, usually consist of a main synchronous machine and an exciter machine that provides the field power to the first one. A rotating diode bridge rectifier is placed between the AC output of the exciter and the main machine's field winding. The excitation system, i.e., the armature of the exciter, the rectifier and the main machine's field winding, rotate together on the same shaft. Therefore, no access is available to the excitation system, thus, when a fault takes place throughout any of the mentioned elements, it should be diagnosed using externally available electromagnetic or mechanical signals. This is a major diagnostic concern in BSM, aside from other common concerns with synchronous machines with static excitation, such as stator interturn short-circuit fault detection.

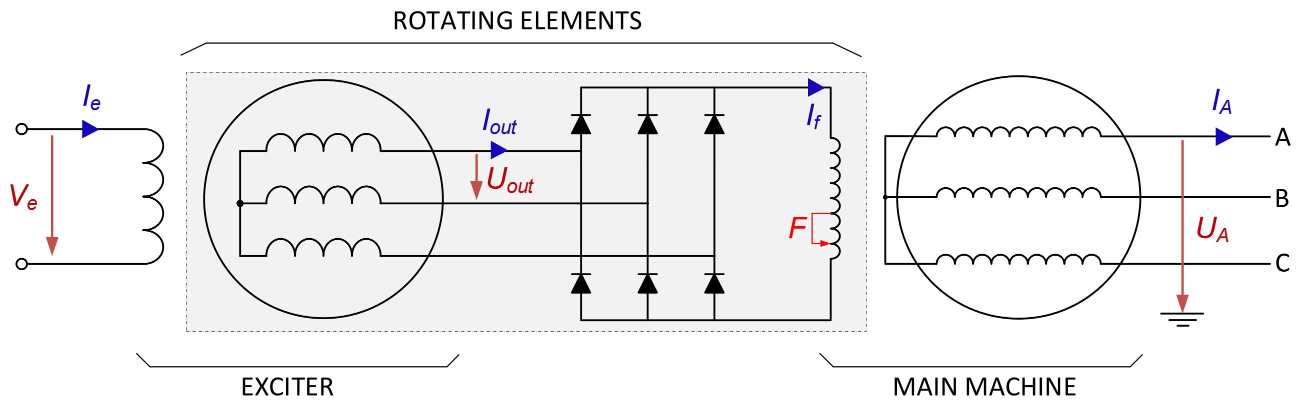

Figure 1. BSM simplified scheme (F: main machine field winding interturn fault).

Different electrical fault types can occur in the excitation system of BSM [10]. In the particular case of interturn short-circuit faults at the main machine's field winding, these shall be carefully considered as magnetomotive unbalance is derived. These faults are represented by F in Figure 1.

In the cases that voltage regulation is performed, the Automatic Voltage Regulator (AVR) [11] seeks to compensate the loss of available turns by increasing the field current in the same proportion, in order to deliver the same average DC rectifier output level and consequently the same magnetomotive force at the field of the main machine.

Therefore, these faults typically lead to a current increase and, consequently, to an increase in the temperature of the field winding, as well as to mechanical oscillations.

The most common specific approaches regarding rotor interturn fault detection at the main field winding of BSM are based on externally available electrical or mechanical signals analysis. The Fast Fourier Transform (FFT) is applied in [12] and the third harmonic of the direct sequence of the current signal is used as an indicator of the presence of rotor interturn short-circuit faults at the field winding of the main machine. In [11], the transfer function between the output voltage and the exciter field current is monitored to detect rotor interturn faults. Alternatively, in [13], the machine's mechanical vibrations under normal and faulty conditions are analyzed through FFT, evidencing the relationship between these and the winding conditions in order to detect the presence of interturn short-circuits.

If a wider scope is considered, beyond BSM but also applicable to these types of machines [14], one of the most-used methods for rotor interturn fault detection in synchronous machines consists of an offline test known as the pole voltage drop test. There are also some popular online rotor interturn fault detection techniques for synchronous machines that are applicable to BSM, such as the ones based on air gap flux analysis [15–17] and on stray flux analysis [18,19], among others.

The most widespread online BSM field winding interturn fault detection methods have been categorized and compared in Table 1.

Table 1. A comparison of various online BSM field winding interturn fault detection methods.

Main Method Categories	Advantages	Disadvantages
Current or voltage signal analysis	Simplicity and accessibility Commonly used equipment (PT, CT) Non-invasiveness Reliability	Low accuracy Measurement errors Electrical noise Computational complexity and cost
Air gap flux analysis	High accuracy Reliability Range of measurements	Invasiveness Installation constraints Machine design constraints Computational complexity and cost
Stray flux analysis	Simplicity of installation Non-invasiveness Range of measurements	Low accuracy Computational complexity and cost

However, it shall be noted that rotor interturn faults usually occur due to turn-to-turn insulation failure. Therefore, insulation monitoring is closely related to these types of faults. The most common insulation failure reasons are related to contamination and to thermal and mechanical stress applied to the rotor windings [20]. Insulation condition can be monitored during maintenance through multiple techniques, such as partial discharge tests. In addition, double slot insulation failures or double rotor-ground faults, i.e., when a ground loop is established after a second rotor-ground fault is produced, when a first rotor-ground fault was already present, can be at the origin of interturn short-circuits. Ground fault detection in BSM [21] can be performed through measurement brushes connected to the field circuit and a ground reference brush, although other online methods have been also developed, such as those based on flux analysis, the measurement of stator currents, the measurement of shaft voltages, twin signal sensing, telemetry or other communication modules [22,23]. Nevertheless, the most common methods to locate the position of a ground fault at the field winding of BSM involve disassembling the machine and measuring the winding insulation at different points.

In addition, there exist some model-based approaches for rotor interturn fault detection in BSM, even though they are scarcer. Model-based fault detection techniques are considered to be more convenient in designing protection schemes if the model is sufficiently accurate. Although electrical dq models have been developed for generators, these are not suitable to work for the complete BSM. Therefore, a different model was used in [24], in which discrete and continuous dynamics were combined to detect rotor interturn faults. In a close reference in [25], a diagnosis criterion was suggested based on the relationship between the variation of the field current and the variation of the reactive power.

In order to overcome the main common disadvantage of electrical signal analysis-based and flux analysis-based methods, which is, according to Table 1, the computational complexity associated with the data acquisition time and the processing time, there is scope for faster online model-based approaches for the condition monitoring of excitation systems of BSM [26].

This paper presents an online fault detection method for rotor interturn faults of BSM, which is based on the comparison between the theoretical and the monitored actual exciter field current at steady state. The theoretical exciter field current calculation rests on a simple healthy excitation system model that takes the main machine stator voltage and current magnitudes as inputs and that applies two calculation stages successively, the first for the main machine and the second for the exciter. The computational simplicity enables real-time online diagnostics. The paper consequently develops a protection method and verifies its suitability for interturn faults at the field winding of the main machine.

The main advantages of the method hereby proposed are that it is non-intrusive, that its inputs are variables that are ordinarily available in the industry, and that it has a low computational complexity derived from the calculation algorithm in use, which is simpler than those used in other methods and more specific than other model-based approaches, enabling fast fault detection and protection. Nevertheless, before applying the proposed method, the machine shall be subjected to conventional testing in order to obtain the parameters needed as an input to compute the theoretical model.

In order to verify the method, computer simulations have been developed, and also a wide range of experimental tests has been performed on a special laboratory setup, for different rotor interturn severity levels. As mentioned before, the fault has the effect of increasing the need for excitation power in order to maintain the same output values. Therefore, the method could be generalized to any other fault in the rotating elements that has a similar effect.

This paper starts with the principles of the proposed technique, which are thoroughly described in Section 2. Section 3 is dedicated to the computer simulations, followed by Section 4, which is dedicated to the experimental tests. Finally, Section 5 concludes with the main original contributions of the work.

2. Operational Principles of the Fault Detection Method

The fault detection method hereby proposed is based on two healthy model stages at a fundamental frequency, one for the main machine and the other for the exciter. As indicated above, the method is non-intrusive and its main distinctive factor is that its inputs are variables that are ordinarily available in the industry (a combination of machine output measurements and the exciter field current measurement), without the need for installing any additional internal or external devices or equipment. Therefore, this method is suitable for preliminary online diagnosis of the excitation system of BSM during operation at steady state, prior to moving onto other further diagnosis techniques.

The main machine model and the exciter model are built upon well-known standard methods, such as the Potier or ASA methods [27]. Therefore, use is made of conventional testing which leads to the attainment of the no-load characteristic, the sustained three-phase short-circuit characteristic and the Potier reactance value. The characteristics are determined from a no-load saturation test and a sustained three-phase short-circuit test, respectively. Moreover, the Potier reactance value determination may additionally need to perform the standard over-excitation test at zero power factor and variable armature voltage. Therefore, the parameters to build the models are easily available through standard testing of the machines.

It shall be noted that the Potier and ASA methods consider the magnetic saturation of the machines, which is more significant in the case of the main machine rather than the exciter, as the latter is usually oversized in order to prevent saturation even if the main machine is overloaded.

2.1. Theoretical Construction of the Healthy Model

2.1.1. First Stage: Main Machine Model

At the first stage, a model of the main machine is constructed. The number of turns of the field winding of the main machine is referred to as N_f. The theoretical main machine field current ($I_{f,cal}$) is computed from the machine output measurements by means of standard methods, such as ASA or Potier at any healthy operating point. These input measurements consist of three out of the following:

- On the one hand, voltage measurements (U_A and/or and/or U_B and/or U_C) and/or current measurements (I_A and/or I_B and/or I_C). Eventually, line voltages (U_{AB} and/or U_{AC} and/or U_{BC}) could be also used instead of phase voltages;
- On the other hand, the active power measurement (P) and/or reactive power measurement (Q). Alternatively, the apparent power measurement (S) could be used as a replacement for either P or Q.

For example, taking the case of the ASA method, the total equivalent field magnetomotive force, m.m.f. ($\mathcal{F}_f$) results from the vector sum of voltage-related ($\vec{\mathcal{F}}_{f,U}$) and current-related ($\vec{\mathcal{F}}_{f,I}$) equivalent m.m.f. and the scalar addition of the m.m.f. related to saturation correction ($\Delta\mathcal{F}_f$), as per Equation (1).

$$\mathcal{F}_f = \left| \vec{\mathcal{F}}_{f,U} + \vec{\mathcal{F}}_{f,I} \right| + \Delta\mathcal{F}_f \tag{1}$$

$$\mathcal{F}_f = N_f \cdot I_{f,cal} \tag{2}$$

As shown in Figure 2, term $\vec{\mathcal{F}}_{f,U}$ represents the equivalent field m.m.f. needed to deliver the given output voltage ($\vec{U}$) at no-load conditions without saturation and it is computed through the airgap line derived from the no-load saturation characteristic, using its slope value m_{airgap}. Term $\vec{\mathcal{F}}_{f,I}$ represents the equivalent field m.m.f. associated with the armature reaction, which is demagnetizing if inductive characterization is assumed, and to the voltage drop at the Potier reactance, and it is computed through the sustained three-phase short-circuit characteristic, using its slope value m_{sc} for the given output current ($\vec{I}$). Finally, term $\Delta\mathcal{F}_f$ represents the additional need of equivalent field m.m.f. due to saturation and it is computed through the difference between the no-load saturation characteristic and the airgap line for the actual delivered e.m.f. (E_r). Equations (3)–(5) correspond to the mentioned terms.

$$\vec{\mathcal{F}}_{f,U} = j \cdot N_f \cdot \left[(m_{airgap})^{-1} \cdot \vec{U} \right] \tag{3}$$

$$\vec{\mathcal{F}}_{f,I} = -N_f \cdot \left[(m_{sc})^{-1} \cdot \vec{I} \right] \tag{4}$$

$$\Delta\mathcal{F}_f = N_f \cdot \Delta I_f \tag{5}$$

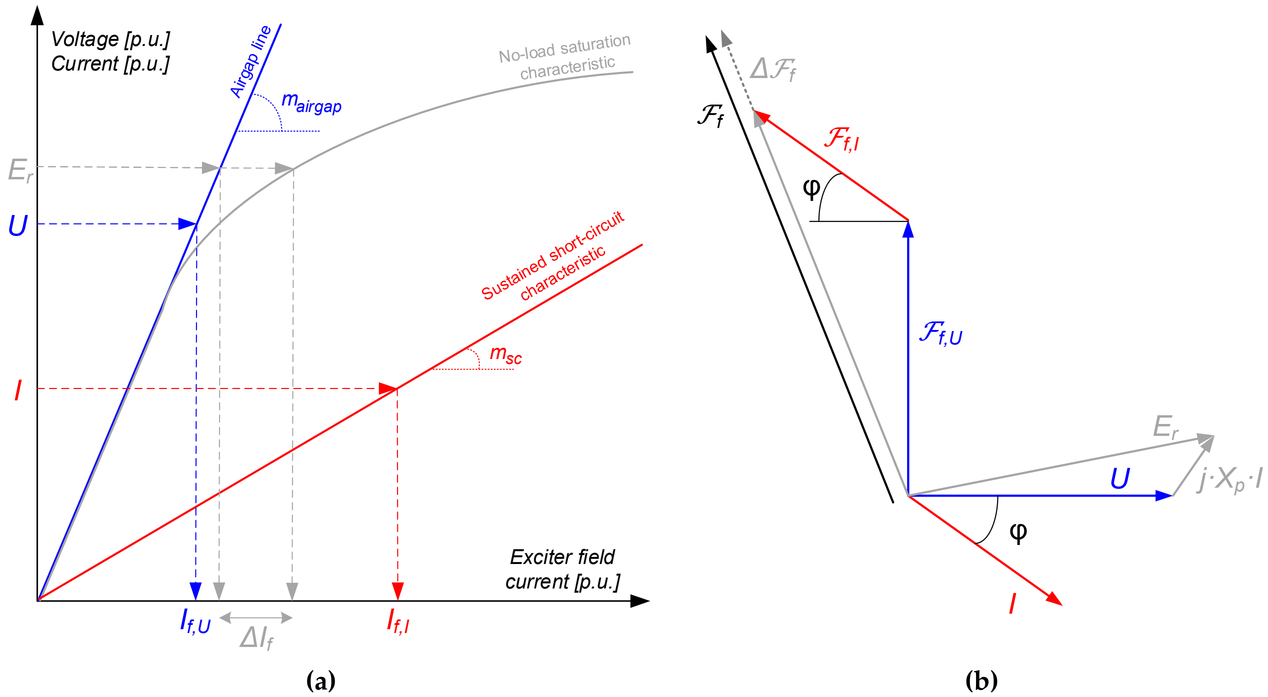

Figure 2. Main machine field current excitation model construction through the ASA method: (**a**) Equivalent exciter field current components determination; (**b**) Phasor diagram.

Finally, the theoretical main machine field current ($I_{f,cal}$) is calculated through the following expression resulting from the phasor composition shown in Figure 2.

$$I_{f,cal} = \Delta I_f + \sqrt{\left[(m_{airgap})^{-1} \cdot U + (m_{sc})^{-1} \cdot I \cdot sin\varphi \right]^2 + \left[(m_{sc})^{-1} \cdot I \cdot cos\varphi \right]^2} \tag{6}$$

where

$$\varphi = arccos\left[\frac{P}{U \cdot I} \right] = arcsin\left[\frac{Q}{U \cdot I} \right] = arctan\left[\frac{Q}{P} \right] \tag{7}$$

2.1.2. Intermediate Rectifier Relationship

It is noteworthy that the full-wave uncontrolled three-phase diode bridge rectifier feeds a highly inductive load which is constantly at a fundamental frequency, consisting of the main machine field winding. Therefore, in healthy conditions, a direct linear relationship can be established between the main machine field current ($I_{f,cal}$) considered as constant DC, and the exciter output current ($I_{out,cal}$) r.m.s., as per Equation (8). Consequently, the theoretical exciter output current in healthy conditions ($I_{out,cal}$) can be directly computed from the theoretical main machine field current ($I_{f,cal}$). The calculation of the exciter output voltage ($U_{out,cal}$) is also unequivocal on the same basis.

$$I_{out,cal} = \sqrt{\frac{1}{2\pi}\cdot\left[\int_0^{\frac{4\pi}{6}}\left(I_{f,cal}\right)^2 d(\omega t) + \int_{\frac{6\pi}{6}}^{\frac{10\pi}{6}}\left(-I_{f,cal}\right)^2 d(\omega t)\right]} = I_{f,cal}\cdot \sqrt{\frac{1}{2\pi}\cdot\left[\frac{4\pi}{6}+\frac{4\pi}{6}\right]} = I_{f,cal}\cdot\sqrt{\frac{2}{3}} \tag{8}$$

2.1.3. Second Stage: Exciter Model

At the second stage, a model of the exciter is constructed in order to calculate the theoretical exciter field current ($I_{e,cal}$). The number of turns of the field winding of the exciter is referred to as N_e. Following the same ASA steps as developed in Section 2.1.1, the general expressions for the exciter model are given by:

$$\mathcal{F}_e = \left|\vec{\mathcal{F}}_{e,U} + \vec{\mathcal{F}}_{e,I}\right| + \Delta\mathcal{F}_e \tag{9}$$

$$\mathcal{F}_e = N_e\cdot I_{e,cal} \tag{10}$$

$$\vec{\mathcal{F}}_{e,U} = j\cdot N_e\cdot\left[\left(m^e_{airgap}\right)^{-1}\cdot \vec{U}_{out,cal}\right] \tag{11}$$

$$\vec{\mathcal{F}}_{e,I} = -N_e\cdot\left[\left(m^e_{sc}\right)^{-1}\cdot \vec{I}_{out,cal}\right] \tag{12}$$

$$\Delta\mathcal{F}_e = N_e\cdot \Delta I_e \tag{13}$$

$$I_{e,cal} = \Delta I_e + \sqrt{\left[\left(m^e_{airgap}\right)^{-1}\cdot U_{out,cal} + \left(m^e_{sc}\right)^{-1}\cdot I_{out,cal}\cdot sin\varphi_e\right]^2 + \left[\left(m^e_{sc}\right)^{-1}\cdot I_{out,cal}\cdot cos\varphi_e\right]^2} \tag{14}$$

However, the general exciter model is largely simplified due to the fact that the load connected to the exciter is comparable to a constant equivalent impedance (Z) at a fundamental frequency, as shown in Figure 3. The equivalent impedance represents the load consisting in the diode bridge rectifier and the main machine field winding, thus being constant both in magnitude (|Z|) and in phase (φ_e) at a fundamental frequency. The equivalent impedance is inductive, then the armature reaction is demagnetizing. The per-phase equivalent impedance can be expressed as per expression 15.

$$Z = |Z|_{\varphi_e} = \frac{\vec{U}_{out,cal}/\sqrt{3}}{\vec{I}_{out,cal}} \tag{15}$$

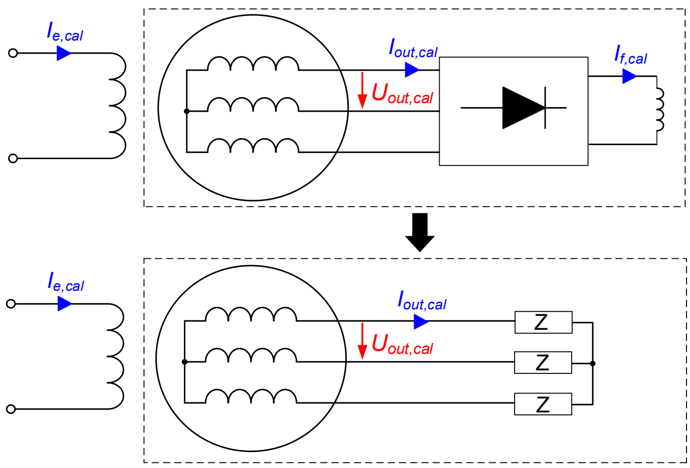

Figure 3. Exciter model (Upper figure: rectifier considered; Bottom figure: equivalent impedance Z simplification). Rotating elements are contained in rectangular sections.

Accordingly, as shown in Figure 4, when the excitation power varies and therefore the exciter output current varies ($I_{out,cal}$ to $I'_{out,cal}$), the same happens for the exciter output voltage ($U_{out,cal}$ to $U'_{out,cal}$), in the same proportion and keeping the same phase shift, so that equivalent impedance Z remains constant both in magnitude ($|Z|$) and in phase (φ_e). As a consequence, both exciter ASA components ($\vec{\mathcal{F}}_{e,U}$ to $\vec{\mathcal{F}}'_{e,U}$ and $\vec{\mathcal{F}}_{e,I}$ to $\vec{\mathcal{F}\prime}_{e,I}$) also vary in the same proportion and maintain their phase difference (θ), given that they stem from linear relationships with the exciter output voltage and the exciter output current, as per expressions 10 and 11, respectively.

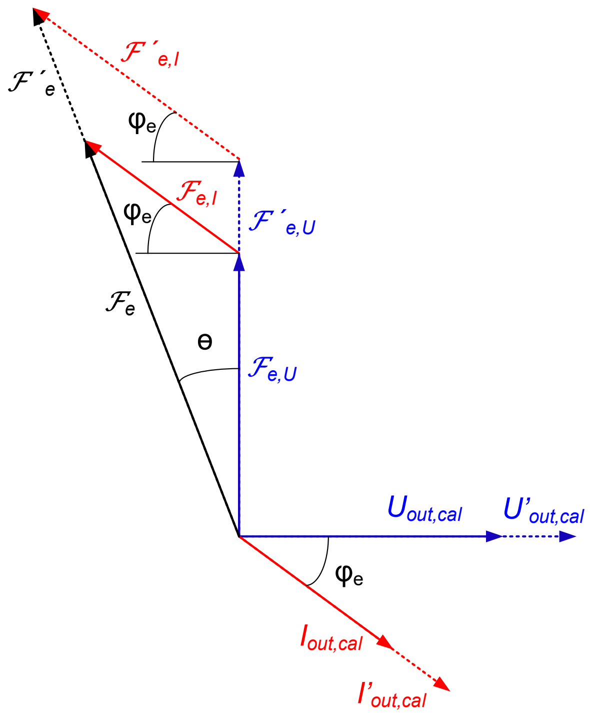

Figure 4. Exciter machine field current calculation by the ASA method. Phasor diagram.

Finally, the exciter total equivalent field m.m.f. increases in the same-mentioned proportion ($\vec{\mathcal{F}}_e$ to $\vec{\mathcal{F}}'_e$) and a direct scalar magnitude relationship is deduced between the exciter output current ($I_{out,cal}$) and the theoretical exciter field current ($I_{e,cal}$), avoiding the general use of expression 14. This way, the method for the exciter is ultimately simplified so that with only $I_{f,cal}$ as an input, $I_{e,cal}$ can be directly linearly computed.

It shall be noted that exciters are usually oversized in order to have a fast transient response in case of increasing the current at the main machine field winding. Therefore, they do not saturate at any expected operating point at the steady state. The non-linearity related to saturation has not been considered in the simplification ($I_{e,cal}$ is considered proportional to $I_{out,cal}$ at any steady state operation point), therefore $\Delta I_e = 0$, even though a scalar component addition could be eventually performed consisting in the difference between the no-load saturation characteristic and the no-load characteristic of the exciter.

Physically, as the effect of the exciter armature reaction depends on the power factor ($cos\varphi_e$), which in addition to being lagging then demagnetizing remains constant, the phase difference between the exciter main field flux (linked to the exciter field poles) and the exciter armature reaction flux, is constant. Therefore, the exciter resultant flux (linked to the final e.m.f. delivered by the exciter) remains with a constant phase shift at any operating point. This interpretation, given that the impedance connected to the exciter is constant, justifies the direct relationship between the magnitudes of the flux components and the exciter load power.

2.2. Fault Detection Method

A schematic layout of the proposed fault detection and protection method is provided in Figure 5. The proposed fault detection method is based on the fact that in case of interturn fault in the field winding, the AVR will call for a greater need of excitation power with respect to the theoretical healthy excitation power, calculated through the two-stage model described in Section 2.1., in order to finally maintain the same machine output setpoints. However, the method is also applicable when the excitation is controlled in manual mode, as it will be developed further on.

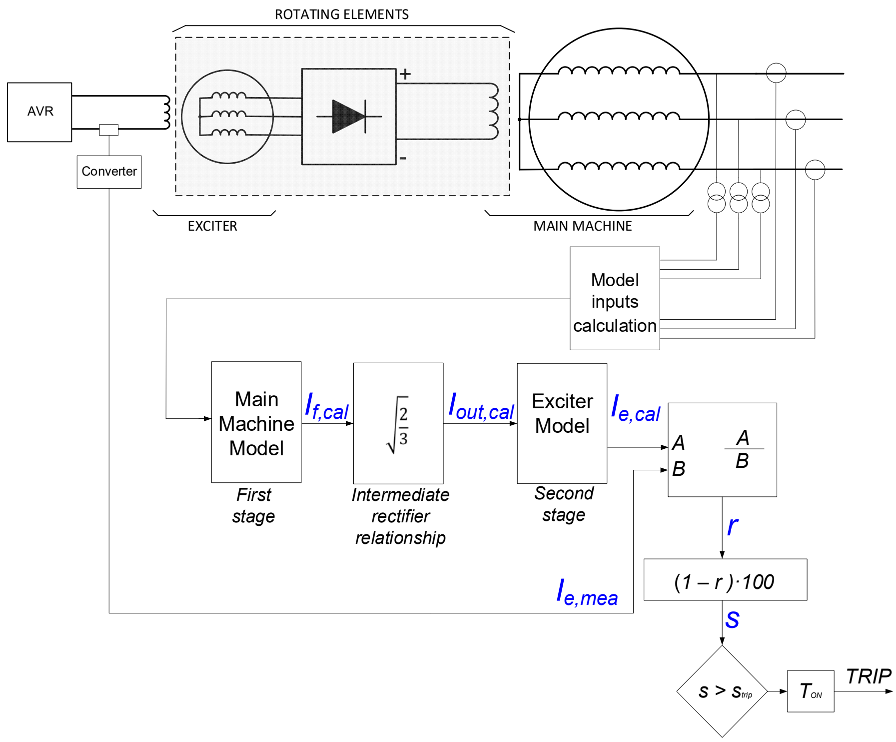

Figure 5. Simplified layout of the detection method for faults in the excitation system of BSM.

The needed inputs consist of discrete measurements that are ordinarily available continuously in industrial applications, as the electrical equipment usually includes voltage and current instrument transformers, wattmeters and varmeters in order to monitor the operating point of the machine at each time. In Figure 5, basic electrical input magnitudes (voltages and currents) on each phase have been represented as an example, obtained through measurement voltage transformers (PT) and measurement current transformers (CT), respectively, although any of the combinations of basic and derived variables as described in Section 2.1.1. would be possible. Regarding the exciter field current measurement, a DC current shunt has been represented, although other techniques, such as a Hall effect sensor, could be also used.

First, the theoretical exciter field current value ($I_{e,cal}$) is estimated through the two-stage healthy condition model, which is summed up in the following calculation steps:

1. Main machine model

The theoretical main machine field current value ($I_{f,cal}$) is estimated through the first stage healthy condition model, through the application of standard methods, such as the ASA method, as per Section 2.1.1. Specifically, Equation (6) provides the desired estimation from the inputs.

2. Intermediate rectifier relationship

The theoretical exciter output current ($I_{out,cal}$) r.m.s. is computed from $I_{f,cal}$ through well-known relationships of the full-wave three-phase diode bridge rectifier, as per Section 2.1.2.

Specifically, Equation (8) provides the value of $I_{out,cal}$ from $I_{f,cal}$ and Equation (15) provides the value of the theoretical exciter output line voltage ($U_{out,cal}$) r.m.s. from $I_{out,cal}$ through a linear relationship.

3. Exciter model

The theoretical exciter field current value ($I_{e,cal}$) is estimated through the second stage healthy condition model, through the application of standard methods, such as the ASA method, as per Section 2.1.3. Specifically, Equation (14) provides the value of $I_{e,cal}$ from $I_{out,cal}$ and $U_{out,cal}$. However, this step could be reduced to a simple linear experimental relationship of $I_{e,cal}$ with $I_{out,cal}$, thus with $I_{f,cal}$, owing to the fact that the load connected to the exciter is comparable to a constant equivalent impedance (Z) at a fundamental frequency.

The obtained value of $I_{e,cal}$ represents the exciter field current that would be necessary if the excitation system was in a healthy condition for the same actual operating point of the BSM. Parameter r represents the ratio, at any certain operating point, between the theoretical exciter field current ($I_{e,cal}$) and the actual measured exciter field current ($I_{e,mea}$), which is usually measured with a shunt or a Hall effect sensor. If $I_{e,mea} > I_{e,mea}$, as in the faulty condition cases, $r < 1$.

In the case of interturn faults in the main machine field winding, the fault severity can be arbitrary inside a certain range depending on the number of shorted turns ($0 < N \leq N_{total}$) or can even increase progressively over time. The greater the proportion of shorted turns (N) with respect to the total number of field winding turns (N_{total}), the fault is said to be more severe.

If the AVR is in operation, it seeks to compensate the mentioned loss of available turns by increasing the exciter field current in the same proportion, in order to deliver the same average DC rectifier output level and consequently the same magnetomotive force at the field of the main machine. Therefore, parameter r coincides with the proportion of shorted turns (N) with respect to the total number of turns (N_{total}). In this case, an increase in $I_{e,mea}$ would be seen while $I_{e,cal}$ remains constant ($r < 1$) as the operating point of the machine remains at the same value.

On the other hand, if the AVR is not in operation, a drop in the output reactive power (Q) is produced, and in this case $I_{e,mea}$ remains at the same value while $I_{e,cal}$ decreases proportionally to the ratio between N and N_{total} ($r < 1$ as well), as the new operating point with a lower reactive power output is considered.

Finally, parameter s represents the percentual fault severity level estimation, i.e., the estimation of the proportion of shorted turns, directly computed from factor r. Equations (16) and (17) gather the definitions of r and s, respectively, through which rotor interturn faults can be detected when $I_{e,mea} > I_{e,cal}$, which leads to $r < 1$ and $s > 0$.

$$r = \frac{N}{N_{total}} = \frac{I_{f,cal}}{I_{f,mea}} \tag{16}$$

$$s = (1 - r)\cdot 100 \tag{17}$$

The resulting severity estimation (s) shall be used in order to trip the machine, or alternatively to give out an alarm or a warning, when a certain threshold (s_{trip}) is attained, which is related to a certain proportion of admissible shorted turns.

The value of $I_{e,cal}$ can be affected by a factor k to perform the calculations, so that the rotor interturn fault detection is carried out based on the following comparison: $I_{e,mea} > k \cdot I_{e,cal}$. The value of factor k shall be set according to the accuracy of the estimation, especially regarding the precision of the measuring devices in use, typically between 1.02 and 1.05 ($k = 1.05$ in the case of the experimental tests described in Section 4). This would be assimilable to applying a factor of safety with the aim of avoiding unwanted trips or alarms in normal conditions due to inaccuracy issues.

A time delay parameter (T_{ON}) shall be accurately set according to the exciter capacity to withstand the fault, generally upon an inverse function with respect to the severity level, among other factors.

The protection method is conceived to cover steady state operating points, because given that each variable has a different transient behavior, the reliability of the theoretical exciter field current estimation method during changes of the operating point is not guaranteed. The protection method may be applied computationally at an industrial level through the use of a Digital Signal Processor (DSP) or a Microprocessor to perform the real-time fault detection automatically.

3. Computer Simulations

3.1. Computer Simulation Model

A Simulink® simulation model was built, as shown in Figure 6, in order to validate the theoretical principles described in the previous section, which are the basis of the healthy model. On this simulation model, numerous healthy and faulty condition tests were carried out in order to check the usefulness of the detection method, for different *[P,Q]* operating points.

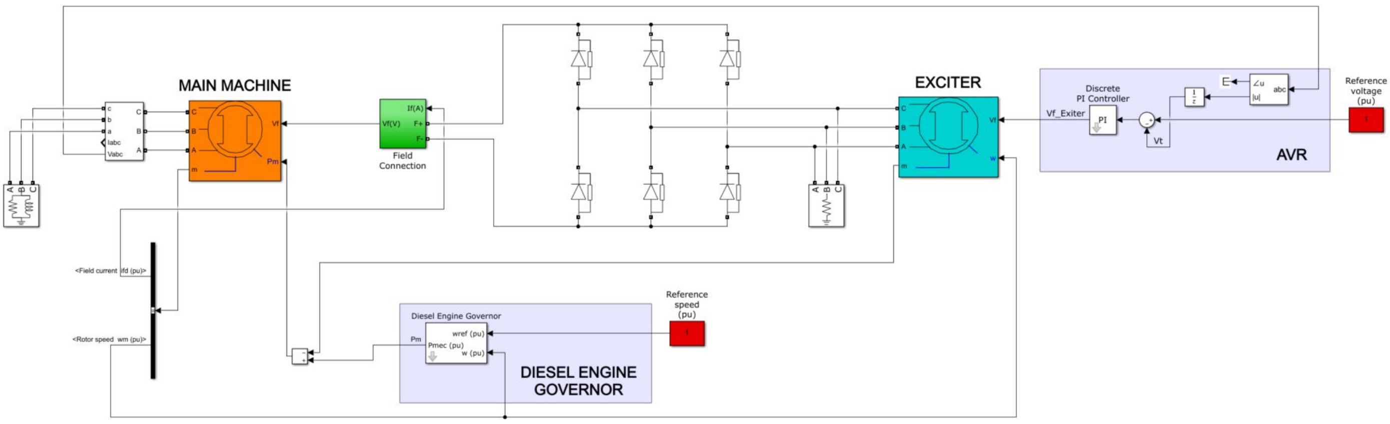

Figure 6. BSM computer simulation model.

3.2. Healthy Condition Simulations

The main purpose of the healthy condition simulations is to verify the excitation system model, specifically the direct magnitude relationship between the theoretical main machine field current ($I_{f,cal}$) and the theoretical exciter field current ($I_{e,cal}$).

First of all, the assumption that the load connected to the exciter is comparable to an equivalent impedance which is constant both in magnitude and in phase shall be verified, as it is the basis of the deduction of the theoretical excitation system model. Therefore, U_{out} and I_{out} waveforms shall be checked for different operating conditions.

As an example, these waveforms are shown for [P_1 = *250 kW*, Q_1 = *0 kvar*] and for [P_2 1500 *kW*, Q_2 = *0 kvar*] in Figure 7. Both waveforms have a heavy sinusoidal component and they are affected by the diode conduction sequence. When the [P_1, Q_1] case is compared to the [P_2, Q_2] case, in which the exciter needs to provide greater excitation power, it can be seen that only an amplitude variation takes place, resulting in ratios $|U_{out}|_1/|I_{out}|_1$ and $|U_{out}|_2/|I_{out}|_2$ remaining essentially constant. This means that the magnitude of the equivalent impedance seen from the output terminals of the exciter is constant. Furthermore, if both cases are compared, there is no meaningful phase shift difference between U_{out} and I_{out} waveforms, which is to say that I_{out} keeps the φ_e delay with reference to U_{out} regardless of the excitation level. It can be concluded that an eventual $Z = |Z|_{\varphi e}$ equivalent resistive-inductive impedance remains constant both in its magnitude and its phase.

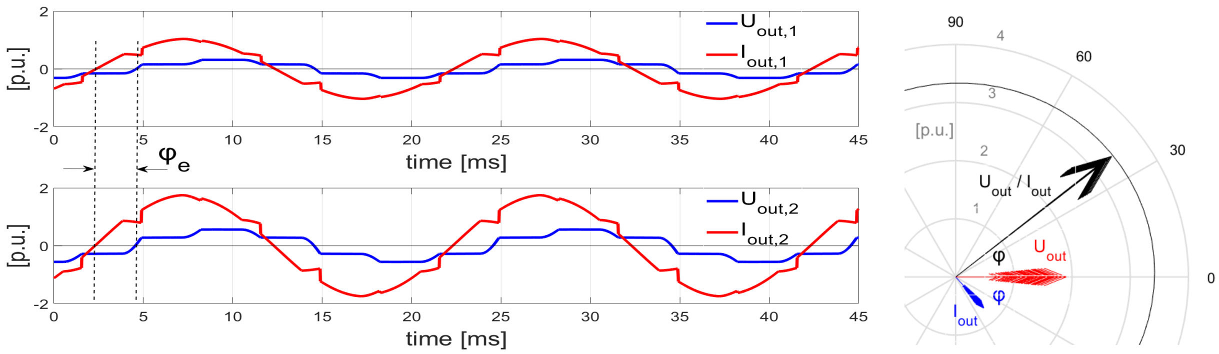

(**a**) (**b**)

Figure 7. Constant impedance equivalence property study: (**a**) Exciter output current (I_{out}) and line voltage (U_{out}) waveforms (Upper Figure: $P_1 = 250\ kW$, $Q_1 = 0\ kvar$ and Bottom Figure: $P_2 = 1500\ kW$, $Q_2 = 0\ kvar$); (**b**) Per-unit phasor diagram.

As an extension, U_{out} and I_{out} phasors resulting from all the performed healthy condition simulations have been gathered in Figure 7, evidencing their proportional growth in magnitude and their constant phase shift regardless of the excitation level.

On the other hand, in order to verify the assumption made on the rectifier bridge model, the relationship between the main machine field current (I_f) and the exciter output current magnitude ($|I_{out}|$) was checked to be linear, as shown in Figure 8.

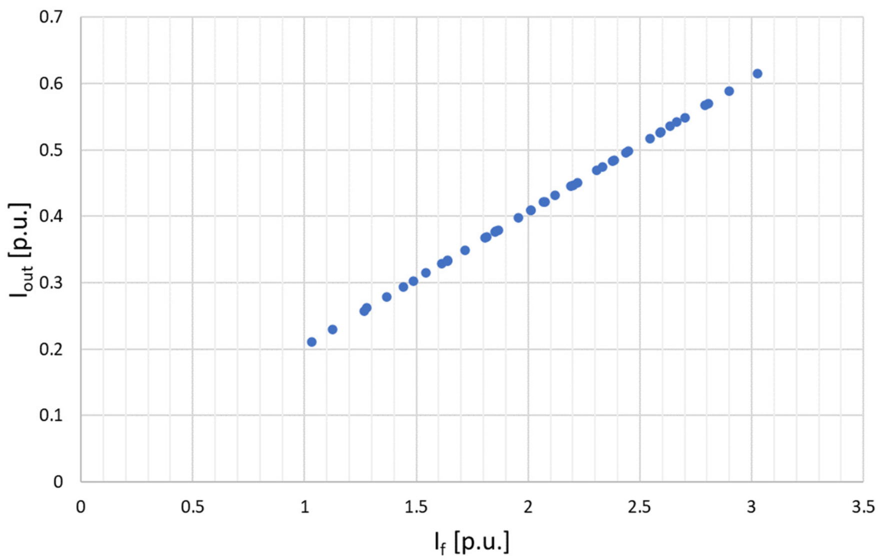

Figure 8. Relationship between I_f (DC) and $|I_{out}|$ (AC rms) for the simulation model exciter.

On the whole, all the results obtained from the performed simulations have been gathered in order to evaluate the relationship between both excitation currents (I_f and I_e), as shown in Figure 9. It is evidenced that the main machine field current (I_f) is proportional to the exciter field current (I_e), leading to the conclusion that the simulations sustain the theoretical developments.

Finally, all healthy condition exciter field current (I_e) simulation results are presented in Figure 10 for different *[P,Q]* operating points at the reference main machine output voltage. It shall be noted that different output voltages result in different parallel surfaces above ($U > 400\ V$ or $1\ p.u.$) or below ($U < 400\ V$ or $1\ p.u.$) the surface shown in the mentioned figure. This healthy set of data is provided as a reference to compare the results in the faulty condition cases for the same operating points in Figure 11.

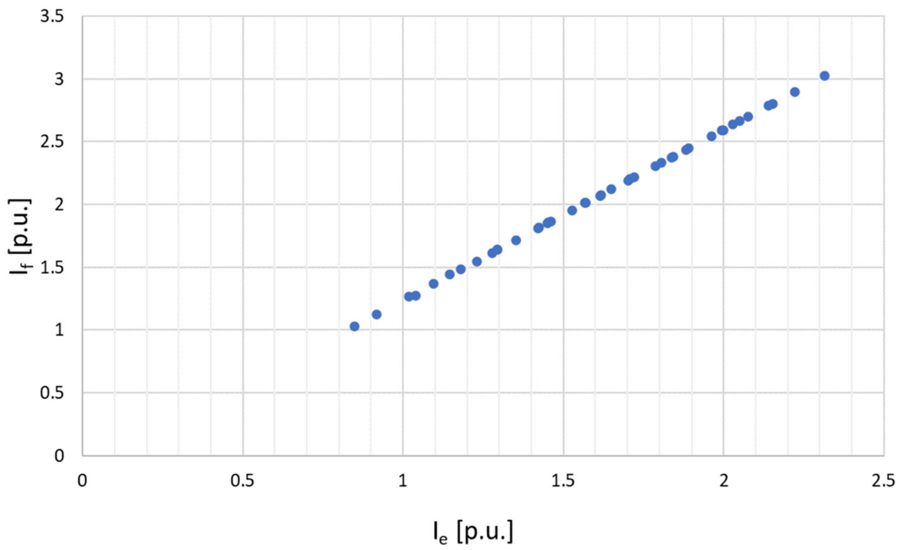

Figure 9. Relationship between I_e (DC) and I_f (DC) for the simulation model exciter.

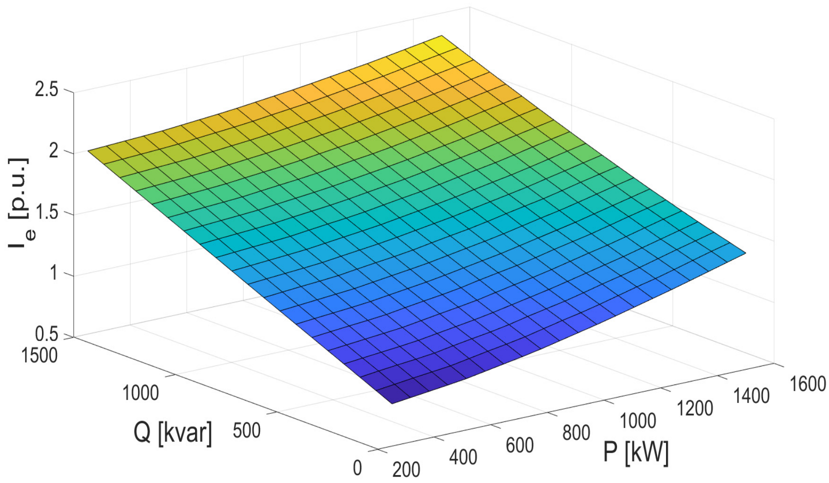

Figure 10. Simulation results. Per-unit exciter field current (I_e) simulation results for different *[P,Q]* operating points at reference output voltage (U = *400 V* or *1 p.u.*) in healthy conditions.

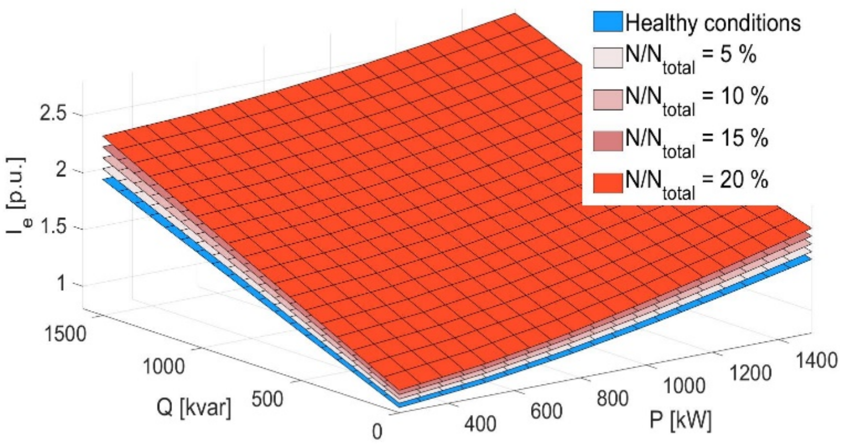

Figure 11. Simulation results. Per-unit exciter field current (I_e) simulation results for different *[P,Q]* operating points at reference output voltage (U = *400 V* or *1 p.u.*) in faulty conditions (interturn faults at the field winding of the main machine, with different severity levels: N/N_{total} = *5, 10, 15 and 20%*).

3.3. Faulty Condition Simulations

Faulty condition tests were carried out to verify the potential of the method to detect electrical faults in the rotating excitation system of BSM, which have in common that they imply a rise in the exciter field current when the AVR system is in service.

Simulations of interturn faults at the field winding of the main machine with different fault severity levels (N/N_{total} = *5, 10, 15 and 20%*) have been performed. The exciter field current (I_e) in case of fault at reference voltage (U = *400 V* or *1 p.u.*) for different *[P,Q]* operating points is presented in Figure 11. The reference healthy case surface provided in Figure 10 is also shown in Figure 11 as a baseline.

As mentioned before, in order to deliver the same magnetomotive force at the field of the main machine and to consequently maintain the same output, the AVR system tends to compensate the loss of available turns by increasing the main machine's field current (I_e) in the same proportion. Therefore, and given that the main machine's field current (I_f) is linear with the exciter field current (I_e) as has been proved, an increase in I_f proportional to the proportion of shorted turns is attained, as shown in Figure 11.

As can be deduced from Figure 11, an appropriate differentiation can be carried out between the faulty condition cases and the healthy case baseline, making straightforward the distinction between the healthy and the faulty condition cases and the fault severity estimation. This fact is made manifestly clear due to the perfectly proportional gaps between parallel surfaces according to the proportion of shorted turns, i.e., in case of a fault the exciter field current exceeds in 5, 10, 15 or 20%, according to N/N_{total}, the healthy analogous operation point.

It shall be noted that if the AVR was not in service, characteristic drops in the output reactive power (Q) would be recognized instead. A new operating point on the faulty condition surface would be attained but for the same exciter field current, and consequently the proportional gaps would be similar.

4. Experimental Tests

4.1. Experimental Setup

A standard practice in BSM testing is to mount temporary slip rings on the rotor in order to enable to take direct measurements in the excitation system. A schematic representation of this arrangement is provided in Figure 12. A representation of the regular arrangement is also provided in the same figure.

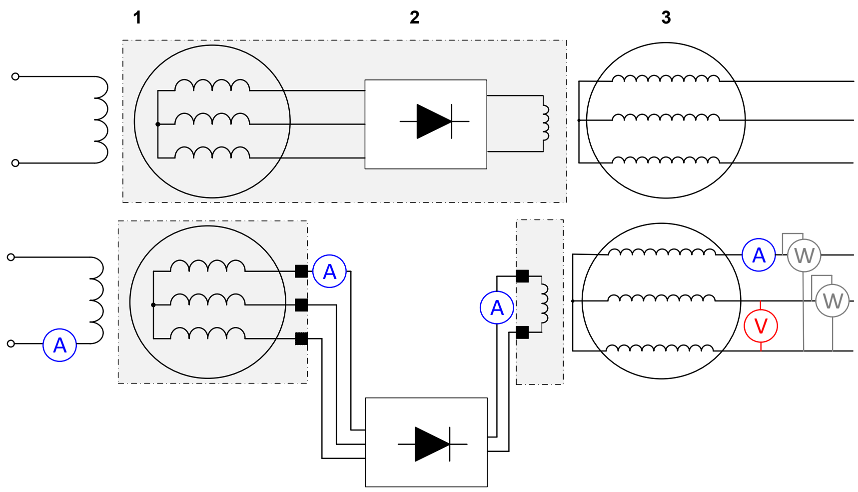

Figure 12. BSM schematic representation. On top, of the regular arrangement, and on the bottom, the experimental setup ((1) Exciter; (2) bridge rectifier; (3) main machine). Rotating elements are contained in gray sections.

The experimental setup, which is shown in Figure 13, includes *(a)* an induction motor that drives the shaft, which is controlled by a variable-frequency drive (VFD), and on its same shaft, *(b)* a BSM, which is excited through a DC variable voltage supply system. A *(c)* diode bridge rectifier with sectional terminal blocks was made static between the exciter and the main machine and *(d)* slip rings were installed for both its inputs and its outputs.

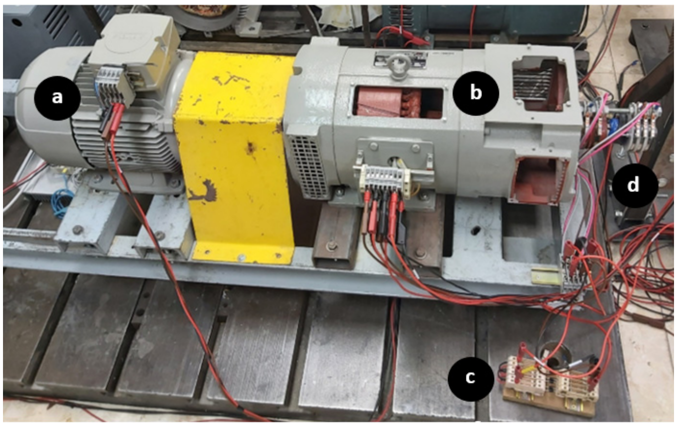

Figure 13. Experimental setup. (**a**) Induction motor; (**b**) generator; (**c**) diode bridge rectifier; (**d**) slip rings and brushes.

The machine is connected to the grid through a transformer and an adjustable AC busbar set. When the machine is paralleled with the grid, active power (P) and reactive power (Q) can be controlled through the VFD and the DC adjustable voltage supply system, respectively. In addition, the grid side voltage (U) can be modified through the adjustable AC busbar set.

The tests were performed on 4-salient poles, 5 kVA, 400 V, BSM. Detailed data about the main synchronous machine and the exciter are provided in Table 2 and Table 3, respectively.

Table 2. Main machine data.

Alternator Type	Synchronous 3-Phase	
Rated power	5	kVA
Rated speed	1500	rpm
Rated voltage	400	V
Rated current	7.2	A
Pole pairs	2	
Rated frequency	50	Hz
IP	21	
Isolation class	F	
Rated excitation voltage	33	V
Rated excitation current	4.10	A

Table 3. Exciter data.

Alternator Type	Synchronous 3-Phase	
Rated power	277	VA
Rated speed	1500	rpm
Rated voltage	40	V
Rated current	4	A
Pole pairs	4	
Rated frequency	100	Hz
IP	21	
Isolation class	F	
Rated excitation voltage	33	V
Rated excitation current	0.61	A

Various measuring instruments were installed at the following points, as can also be seen in Figure 12:

1. An ammeter at the excitation DC input of the exciter;
2. An ammeter at the three-phase connection between the exciter and the rectifier;
3. An ammeter at the DC connection between the rectifier and the main machine field winding;
4. Three-phase voltage and current sensors and a wattmeter at the output of the main machine.

4.2. Healthy Condition Tests

The BSM has been tested in healthy conditions in a wide range of operating conditions. A set of 1575 healthy condition tests were performed for in the range of $0 \leq P \leq 1500\ W$ and $-1000 \leq Q \leq 2500\ var$, with grid side voltages in the range of $320 \leq U \leq 420\ V$. As it can be inferred, the healthy condition tests have covered generator operation, from under-excited to over-excited conditions, at different grid side voltage values.

The main machine model having been verified in previous works through standard methods [28], the excitation system model description made in Section 2.1.2., based on the direct magnitude relationship between the estimated main machine field current ($I_{f,cal}$) and the estimated exciter field current ($I_{e,cal}$), shall be experimentally verified. The relationship between the main machine actual field current ($I_{f,mea}$), which is directly measurable in the special experimental setup, and the exciter actual field current ($I_{e,mea}$), was studied for all the healthy condition tests. The result is shown in Figure 14, drawing the conclusion that the experimental tests evidence the aforementioned theoretical developments.

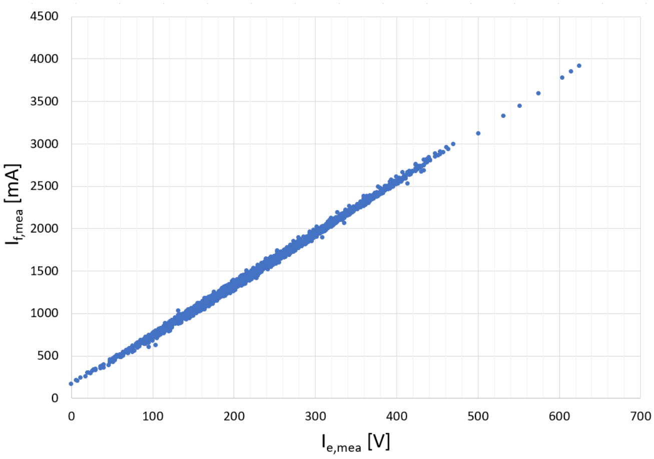

Figure 14. Experimental results. The relationship between the measured main machine field current ($I_{f,mea}$) and the measured exciter field current ($I_{e,mea}$) for all the experimental healthy condition tests.

On the other hand, the results of the healthy condition tests provide a valuable set of reference experimental data which consists of the value of the actual measured exciter field current ($I_{e,mea}$) values for different *[P,Q]* operating points, at different grid side voltage values. Some exciter field current measurements in healthy conditions are presented in Figure 15 for different *[P,Q]* operating points at rated output voltage ($U = 400\ V$). It shall be noted that different output voltages result in different parallel surfaces above ($U > 400\ V$) or below ($U < 400\ V$) the shown surface.

The data provided in Figure 15 may be used to assess the accuracy of the estimation method when actual measured exciter field current values ($I_{e,mea}$) are compared to the theoretical exciter field current value ($I_{e,cal}$) computed through the two-stage healthy condition model for each healthy operating point. The relative errors with respect to $I_{e,mea}$ obtained from this comparison are represented in Figure 16 for each *[P,Q]* operating point at rated output voltage ($U = 400\ V$).

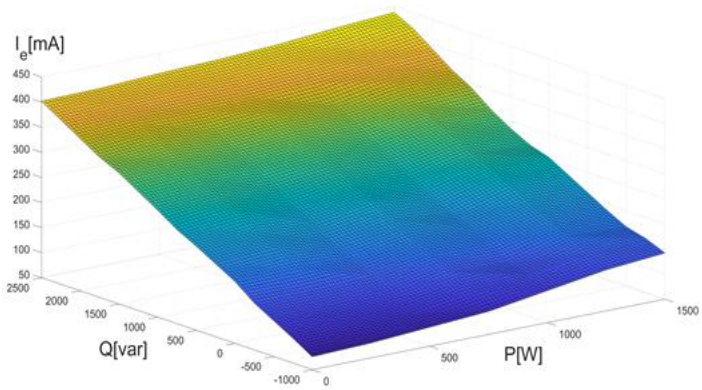

Figure 15. Experimental results. Measured exciter field current ($I_{e,mea}$) for different *[P,Q]* operating points at the rated output voltage *(U = 400 V)* in healthy conditions.

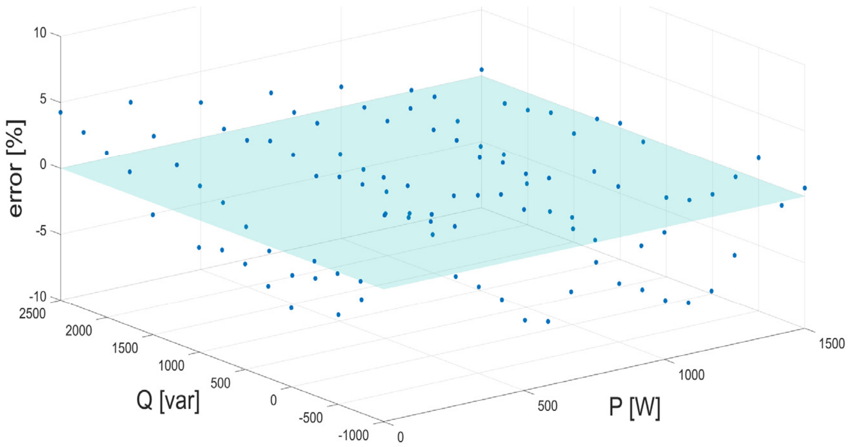

Figure 16. Experimental results. Healthy theoretical model relative errors (%) with respect to the actual measurements collected from healthy condition tests, for different *[P,Q]* operating points at rated output voltage (*U = 400 V*).

As shown in Figure 16, for operation points at rated output voltage (*U = 400 V*), the errors committed do not exceed 6% in any case. In general, the errors are more notable for low output voltage and low output power, because with low voltage and current magnitude values at the exciter field winding (voltages and currents that hardly reach 1 V and 10 mA, respectively), relative errors shoot up, given the sensitivity of the measuring devices. The numerical values are displayed in Table 4.

The obtained estimation confidence intervals are deemed acceptable for fault detection use. In any case, in industrial applications synchronous machines tend to operate in a steady state inside a specific operating region characterized by a minimum output active power and overexcited conditions, which means that the use of specific sub-models can be considered in different operating regions. This sub-model approach would lead to higher accuracy levels, which is desirable in order to avoid false fault detections or trips in the case of electrical faults that imply low increments in the excitation power (if AVR system is in service) or low drops in the output reactive power (if AVR system is not in service).

Moreover, it shall be noted that when relative errors are studied, it is realized that the main machine model is responsible for the main contributions to the overall two-stage model performance errors, which is to say that the fact of linking the main machine model with the exciter model under the theoretical developments does not introduce any significant estimation errors.

Table 4. Experimental results. Healthy theoretical model relative errors (%) with respect to the actual measurements collected from healthy condition tests, for different *[P,Q]* operating points at rated output voltage (U = *400 V*).

P [W], Q [var]	***0***	***250***	***500***	***750***	***1000***	***1250***	***1500***
−1000	*0.85%*	*−0.77%*	*−1.83%*	*−1.03%*	*−4.25%*	*−4.88%*	*−3.51%*
−750	*−1.23%*	*−0.31%*	*−0.73%*	*−4.29%*	*−4.14%*	*−5.01%*	*−4.10%*
−500	*0.36%*	*0.87%*	*−0.60%*	*−5.96%*	*−2.39%*	*−5.84%*	*−2.20%*
−250	*1.87%*	*−1.53%*	*−2.17%*	*−5.80%*	*−5.12%*	*−5.99%*	*−4.07%*
0	*−1.54%*	*−1.70%*	*−2.53%*	*−4.65%*	*−4.32%*	*−5.85%*	*−5.57%*
250	*−0.89%*	*−2.73%*	*−3.56%*	*−4.38%*	*−2.83%*	*−5.54%*	*−5.14%*
500	*0.48%*	*−0.65%*	*−2.51%*	*−4.61%*	*−2.40%*	*−5.32%*	*−5.17%*
750	*0.45%*	*−1.42%*	*−1.96%*	*−2.51%*	*−2.20%*	*−4.41%*	*−2.97%*
1000	*−0.41%*	*−1.63%*	*−1.23%*	*−1.62%*	*−2.19%*	*−3.81%*	*−2.34%*
1250	*−0.07%*	*−0.02%*	*−1.49%*	*−1.21%*	*−1.70%*	*−3.01%*	*−1.79%*
1500	*0.17%*	*−0.01%*	*0.04%*	*−0.49%*	*−0.94%*	*−2.10%*	*−3.46%*
1750	*1.50%*	*0.24%*	*−0.01%*	*−0.24%*	*−0.04%*	*−2.25%*	*−2.21%*
2000	*2.80%*	*0.56%*	*0.07%*	*1.09%*	*−0.97%*	*−1.11%*	*−2.16%*
2250	*3.22%*	*1.68%*	*0.47%*	*1.21%*	*−0.62%*	*0.12%*	*−2.03%*
2500	*3.88%*	*3.21%*	*2.49%*	*5.75%*	*0.95%*	*−0.19%*	*0.01%*

4.3. Faulty Condition Tests

Faulty condition tests were carried out with the main purpose of verifying the potential of the proposed approach to detect interturn faults at the main machine field winding of BSM (with proportion of shorted turns N/N_{total}).

These tests have been performed through the connection of different resistors parallel with a rotor pole winding, so as to decrease the current flow through it in the desired proportion, as shown in Figure 17. The field current flow reduction through the mentioned pole has an equivalent effect to shorting a certain number of turns, which is the decrease in the field m.m.f. (ampere-turns) provided by the pole. Accordingly, faulty condition tests have been performed for different percentual fault severity levels: N/N_{total} = *4.36, 7.40, 11.17 and 15.91%*, given the relationships provided in Table 5.

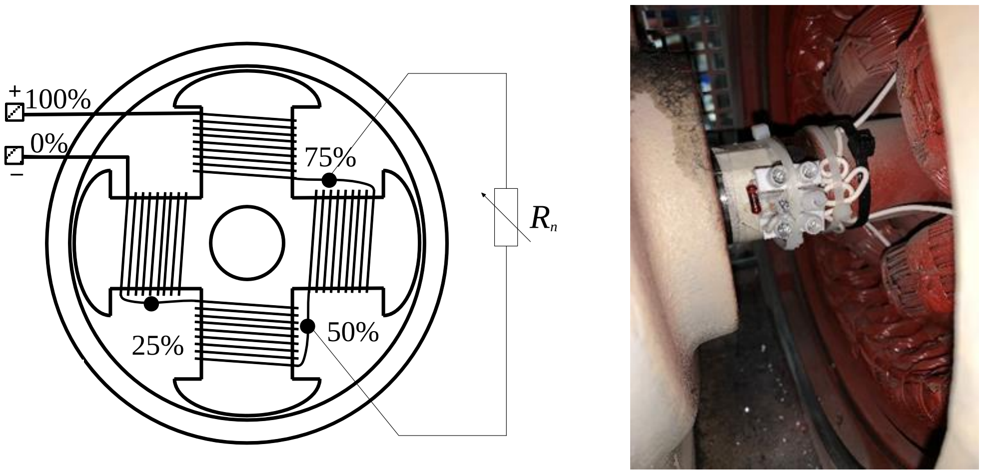

(**a**) (**b**)

Figure 17. Main machine field winding experimental connection in order to perform interturn faults with different parallel resistors with R_n values: (**a**) Schema; (**b**) Connection.

The results for P = *1000 W* at constant voltage (U = *385 V*) are shown in Figure 18. The exciter field current measurements for each of the previous faults are referred to as $I_{e,mea,F,4\cdot 36\%}$, $I_{e,mea,F,7\cdot 40\%}$, $I_{e,mea,F,11\cdot 17\%}$ and $I_{e,mea,F,15\cdot 91\%}$. In addition, the exciter field current measurements in healthy conditions are provided in the same figure and are referred to as $I_{e,mea,healthy}$.

Table 5. Relationships between the parallel resistor value (R_n) and the equivalent proportion of shorted turns (N) with respect to the whole field winding (N_{total}). The whole field winding constitutes a *12.6* Ω total impedance.

R_n [Ω]	N/N_{total} [%]
1.8	15.91
3.9	11.17
7.5	7.40
14.9	4.36

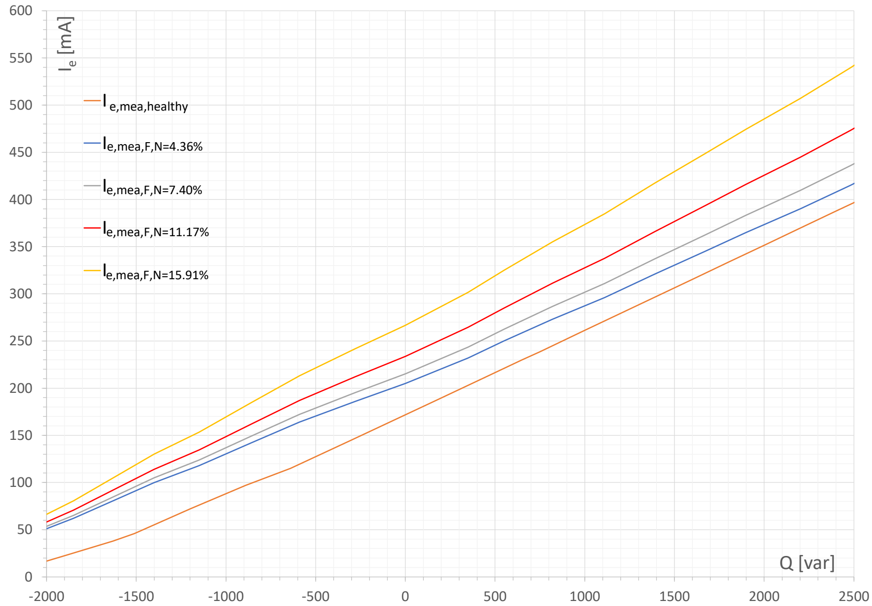

Figure 18. Exciter field current measurements for [*P = 1000 W, Q*], at fixed output voltage (*U = 385 V*) in healthy and main field winding interturn fault conditions.

As can be deduced from Figure 18, an appropriate differentiation can be carried out between the healthy condition case and the faulty condition cases. This fact is made manifestly clear due to the gaps between the lines in healthy and faulty conditions, which is wider for higher Q values. Moreover, the proportional increase in the needed exciter field current with the proportion of shorted turns (N/N_{total}) is verified through the experimental approach.

5. Conclusions

This paper presents a new model-based detection method for interturn faults at the field winding of the main machine.

The proposed method is based on the comparison of the actual measured exciter field current and the theoretical exciter field current calculated, at each operating point. The theoretical exciter field current is computed through a two-stage model for healthy conditions from the machine output measurements.

At the first stage, a model of the main machine is used. The main machine theoretical field current is computed from the machine output measurements using one of the well-known standard methods, such as the ASA or Potier methods.

At the second stage, a model of the exciter is used. From the main machine theoretical excitation current, a model of the exciter is proposed in order to calculate the exciter field current using several verified properties. Among these properties, it shall be remarked that given the characterization of an analogous equivalent load connected to the exciter, with constant magnitude and power factor, it is possible to move from a vector relationship to a direct scalar relationship between the exciter field current and the exciter output current.

The advantages of this new method are its non-intrusiveness and the ordinary availability of the required signals in industrial applications such as in power plants. Moreover, it needs a shorter computational time in comparison with other monitoring techniques.

The use of the method to provide an indication in the event of interturn fault in the field winding is of particular interest for the operator as a first online strategy, before moving to further diagnosis methods. The fault detection method has been validated with consistent results through computer simulations and through experimental tests that were carried out on a special laboratory setup.

For further works, the method could be extended to the detection of any electrical fault throughout the rotating excitation system, such as diode faults or loose connections which render out of service a branch of the rectifier, as all of them imply a difference between the measured and the theoretical exciter field current. Fault classification techniques after detection could also be complemented with other diagnostics techniques for precise fault location throughout the rotating excitation system.

Author Contributions: Conceptualization, K.M. and C.A.P.; methodology, K.M. and C.A.P.; software, K.M.; validation, K.M. and L.F.B.; formal analysis, K.M. and L.F.B.; investigation, K.M., L.F.B. and C.A.P.; resources, K.M.; data curation, K.M.; writing—original draft preparation, K.M.; writing—review and editing, K.M., J.M.G., L.F.B. and C.A.P.; visualization, K.M., J.M.G., L.F.B. and C.A.P.; supervision, L.F.B.; project administration, C.A.P.; funding acquisition, C.A.P. All authors have read and agreed to the published version of the manuscript.

Funding: This research received no external funding.

Data Availability Statement: Not applicable.

Conflicts of Interest: The authors declare no conflict of interest.

References

1. Juan, Y.; Haiyi, X.; Zhangang, Y. An Active Control Excitation Method of Three-Stage Brushless Synchronous Starter/Generator in Electric Starting Mode for MEA. *IEEE Access* **2021**, *9*, 109763–109774. [CrossRef]
2. Basak, S.; Mondal, A.K.; Chakraborty, C. Performance and Analysis of a New Brushless Synchronous Generator for DC Microgrid Application. *IEEE Trans. Ind. Appl.* **2020**, *56*, 3137–3148. [CrossRef]
3. Jiao, N.; Sun, C.; Zhang, X.; Duan, X.; Liu, W. Double-Side Voltage-Behind-Reactance Model of Brushless Exciter in Aircraft Wound-Rotor Synchronous Starter-Generator Considering Magnetic Saturation. *IEEE Trans. Energy Convers.* **2021**, *36*, 2358–2369. [CrossRef]
4. Sikora, A.; Zielonka, A.; Woźniak, M. Minimization of Energy Losses in the BLDC Motor for Improved Control and Power Supply of the System under Static Load. *Sensors* **2022**, *22*, 1058. [CrossRef] [PubMed]
5. Chapman, S.J. *Electric Machinery Fundamentals*, 5th ed.; McGraw-Hill: New York, NY, USA, 2012; ISBN 9780073529547.
6. *IEEE Std C37 102-2006 (Revision of IEEE Std C37 102-1995)*; IEEE Guide for AC Generator Protection. IEEE: New York, NY, USA, 2006; pp. 1–177. [CrossRef]
7. Gupta, S.; Charola, P.; Patel, B. Field Experience on Effect of Power Electronic Component Failure in Excitation Circuit of a 5 MW Synchronous Motor. In Proceedings of the 2018 IEEE International Conference on Power Electronics, Drives and Energy Systems (PEDES), Chennai, India, 18–21 December 2018; pp. 1–6.
8. Nøland, J.K.; Nuzzo, S.; Tessarolo, A.; Alves, E.F. Excitation System Technologies for Wound-Field Synchronous Machines: Survey of Solutions and Evolving Trends. *IEEE Access* **2019**, *7*, 109699–109718. [CrossRef]
9. Pallantla, M.; Kumar, P.; Mohan, N. Comparison and Evaluation of the Different Brushless Excitation Topologies for Synchronous Machines-A Literature Survey. In Proceedings of the 2020 IEEE International Conference on Power Electronics, Smart Grid and Renewable Energy (PESGRE2020), Cochin, India, 2–4 January 2020; pp. 1–6.
10. Kim, H.J.; Shaikh, M.F.; Lee, S.B.; Platero, C.A.; Kim, T. Alternative Test Methods for Monitoring the Condition of Brushless Exciters in Synchronous Machines. *IEEE Trans. Energy Convers.* **2022**, *37*, 2009–2018. [CrossRef]
11. Batzel, T.D.; Swanson, D.C.; Defenbaugh, J.F. Predictive diagnostics for the main field winding and rotating rectifier assembly in the brushless synchronous generator. In Proceedings of the 4th IEEE International Symposium on Diagnostics for Electric Machines, Power Electronics and Drives (SDEMPED), Atlanta, GA, USA, 24–26 August 2003; pp. 349–354.
12. Sottile, J.; Trutt, F.C.; Leedy, A.W. Condition Monitoring of Brushless Three-phase Synchronous Generators with Stator Winding or Rotor Circuit Deterioration. *IEEE Trans. Ind. Appl.* **2006**, *42*, 1209–1215. [CrossRef]

13. Trutt, F.C.; Sottile, J.; Kohler, J.L. Detection of AC Machine Winding Deterioration Using Electrically Excited Vibrations. *IEEE Trans. Ind. Appl.* **2001**, *37*, 10–14. [CrossRef]
14. Guillén, C.E.G.; de Porras Cosano, A.M.; Tian, P.; Diaz, J.C.; Zarzo, A.; Platero, C.A. Synchronous Machines Field Winding Turn-to-Turn Fault Severity Estimation Through Machine Learning Regression Algorithms. *IEEE Trans. Energy Convers.* **2022**, *37*, 2227–2235. [CrossRef]
15. Park, Y.; Lee, S.B.; Yun, J.; Šašić, M.; Stone, G.C. Air Gap Flux-Based Detection and Classification of Damper Bar and Field Winding Faults in Salient Pole Synchronous Motors. *IEEE Trans. Ind. Appl.* **2020**, *56*, 3506–3515. [CrossRef]
16. Yun, J.; Lee, S.B.; Šašić, M.; Stone, G.C. Reliable Flux-Based Detection of Field Winding Failures for Salient Pole Synchronous Generators. *IEEE Trans. Energy Convers.* **2019**, *34*, 1715–1718. [CrossRef]
17. Yun, J.; Park, S.; Yang, C.; Park, Y.; Lee, S.B.; Šašić, M.; Stone, G.C. Comprehensive Monitoring of Field Winding Short Circuits for Salient Pole Synchronous Motors. *IEEE Trans. Energy Convers.* **2019**, *34*, 1686–1694. [CrossRef]
18. Cuevas, M.; Romary, R.; Lecointe, J.; Morganti, F.; Jacq, T. Noninvasive Detection of Winding Short-Circuit Faults in Salient Pole Synchronous Machine with Squirrel-Cage Damper. *IEEE Trans. Ind. Appl.* **2018**, *54*, 5988–5997. [CrossRef]
19. Shaikh, M.F.; Park, J.; Lee, S.B. A Non-Intrusive Leakage Flux Based Method for Detecting Rotor Faults in the Starting Transient of Salient Pole Synchronous Motors. *IEEE Trans. Energy Convers.* **2021**, *36*, 1262–1270. [CrossRef]
20. Stone, G.; Boulter, E.A.; Culbert, I.; Dhirani, H. *Electrical Insulation for Rotating Machines: Design, Evaluation, Aging, Testing, and Repair*, 4th ed.; Wiley-IEEE Press: Piscataway, NJ, USA, 2004; pp. 1–41. ISBN 9780471445067.
21. Pardo, M.A.; Mahtani, K.; Platero, C.A.; Sánchez-Fernández, J.A. New On-line Rotor Ground Fault Location Method for Brushless Synchronous Generators. In Proceedings of the IEEE 13th International Symposium on Diagnostics for Electrical Machines, Power Electronics and Drives (SDEMPED), Dallas, TX, USA, 22–25 August 2021; pp. 140–145.
22. Maughan, C.V.; Reschovsky, J.M. Advances in Motor and Generator Rotor Health. In Proceedings of the IEEE International Symposium on Electrical Insulation, San Diego, CA, USA, 6–9 June 2010; pp. 1–4.
23. Kumar, P.S.; Xie, L.; Thiha, K.; Soong, B.H.; Vaiyapuri, V.; Nadarajan, S. Rotor Mounted Wireless Sensors for Condition Monitoring of Brushless Synchronous Generator. In Proceedings of the 43rd Annual Conference of the IEEE Industrial Electronics Society (IECON 2017), Beijing, China, 29 October–1 November 2017; pp. 3221–3226.
24. Tantawy, A.; Koutsoukos, X.; Biswas, G. Aircraft Power Generators: Hybrid Modeling and Simulation for Fault Detection. *IEEE Trans. Aerosp. Electron. Syst.* **2012**, *48*, 552–571. [CrossRef]
25. Yong-Gang, L.; Ming-Han, M.; Yu-Cai, W.; Guo-Bang, B. The New Criterion of Brushless Excitation Generator Rotor Winding Inter-Turn Short Circuit Fault Diagnosis Based on Reactive Relative Deviation. In Proceedings of the 19th International Conference on Electrical Machines and Systems (ICEMS), Chiba, Japan, 13–16 November 2016; pp. 1–4.
26. Mahtani, K.; Guerrero, J.M.; Beites, L.F.; Platero, C.A. Model-based On-line Protection Method for Brushless Synchronous Generators. In Proceedings of the IEEE 13th International Symposium on Diagnostics for Electrical Machines, Power Electronics and Drives (SDEMPED), Dallas, TX, USA, 22–25 August 2021; pp. 126–132.
27. *EN-IEC 60034-4-1: 2018*; Rotating Electrical Machines—Part 4–1: Methods for Determining Electrically Excited Synchronous Machine Quantities from Tests. International Electrotechnical Commission: Geneva, Switzerland, 2018.
28. Tian, P.; Platero, C.A.; Gyftakis, K.N. On-line Turn-to-Turn Protection Method of the Synchronous Machines Field Winding. In Proceedings of the IEEE 12th International Symposium on Diagnostics for Electrical Machines, Power Electronics and Drives (SDEMPED), Toulouse, France, 27–30 August 2019; pp. 69–74.